

# Laboratory Investigation of Coupled Electrical Interaction of Fracturing Rock with Gases

Yuji Enomoto (✉ [enomoto@shinshu-u.ac.jp](mailto:enomoto@shinshu-u.ac.jp))

Shinshu Daigaku <https://orcid.org/0000-0002-4119-0088>

Tsuneaki Yamabe

Shinshu Daigaku - Asahi Campus: Shinshu Daigaku

Shigeki Sugiura

Genesis Research Institute Inc, Nagoya

Hiroshi Kondo

Genesis Research Institute Inc, Nagoya

---

## Express Letter

**Keywords:** Seismo-electromagnetics, fault valve, rock fracture, deep Earth gas, exo-electron emission

**Posted Date:** January 20th, 2021

**DOI:** <https://doi.org/10.21203/rs.3.rs-150348/v1>

**License:** © ⓘ This work is licensed under a Creative Commons Attribution 4.0 International License.

[Read Full License](#)

---

**Version of Record:** A version of this preprint was published at Earth, Planets and Space on April 15th, 2021. See the published version at <https://doi.org/10.1186/s40623-021-01416-1>.

# Abstract

In the coupled electric interaction of rock fractures and gas invasion, that is, when gases interact with newly created cracked surfaces, the unpaired electrons within the rock crystal defects are thermally stimulated, released into the crack due to the temperature rise at the crack tip via plastic work, and attached to ambient gas molecules to electrify them in a negative state. Using a working hypothesis that this mechanism is the source mechanism of seismo-electromagnetic phenomena, we conducted laboratory experiments in which rocks were fractured with pressurized N<sub>2</sub>, CO<sub>2</sub>, CH<sub>4</sub>, and hot water vapour. Fractures were induced by a flat-ended indenter equipped with a flow channel, which was loaded against blocks of quartz diorite, gabbro, basalt, and granite. Fracture-induced negatively electrified gas currents at 25 °C and 160 °C were successfully measured for approximately a hundred microseconds or more after full development of the crack. The peak electric currents were as high as 0.05–3 mA, depending on the rock species and interaction area of fractured rock and gas and to a lesser extent on the gas species and temperature. The peak current from fracturing granite, which showed higher g-ray activity, was at least 10 times higher than that from fracturing gabbro, quartz diorite, and basalt. The results supported the validity of the present working hypothesis, that coupled interaction of fracturing rock with deep Earth gases during quasi-static rupture of rocks in the focal zone of a fault might play an important role in the generation of pre- and co-seismic electromagnetic phenomena.

## Introduction

Geophysical evidence suggests that deep Earth fluids/gases along fault planes have an important role in generating earthquakes and is this significant for modelling earthquake occurrence. According to the deep Earth gas hypothesis, when water-bearing porous sediment extends to a great depth, the different pressure gradients in water and rock form a stepwise pressure distribution that builds up in the underground rock-water system. Then, a pore-collapsed domain develops at a critical depth and forms an impermeable barrier to deep Earth fluids (Gold 1987; Sibson 1990). An impermeable layer that crosses a high-angle reverse fault is called a “fault valve” (Sibson 1990), and deep Earth fluids can be stored in the lower portions of a fault valve during interseismic periods. Water has been found in deep scientific boreholes to depths up to 10 km, and it is likely that water extends as deep as ~ 20 km in stable crust (Smithson et al. 2000). Meanwhile, the seismogenic zone of on-shore earthquakes commonly also extends to depths of 10–20 km (Sibson 1990).

When both the tectonic shear stress and the pressure of the reservoir fluids reach a critical level, micro-cracks grow in the fault-valve zone and link with each other. Then, when the linked cracks breach the fluid reservoir barrier, low-viscosity gases, such as hydrocarbons and <sup>3</sup>He contained in the deep Earth fluids, percolate into the linked cracks, widen them, and weaken the seismogenic zone, which results in acceleration of unstable ruptures leading to strong earthquakes. In fact, recent observation of helium/argon isotope changes after the 2016 Kumamoto earthquake, which was a high-angle reverse-type event, suggested that the helium/argon anomaly probably resulted from deep-seated fluids being squeezed through the fault plane by the tectonic stress that caused the earthquake (Sano et al. 2016).

The beginning of a quasi-static rupture of the seismogenic fault-valve zone when the linked cracks breach the fluid reservoir, leading to the unstable acceleration of rupture of the whole seismogenic zone, might correspond to a precursor period of earthquakes.

The fault-valve model is also assumed to apply at subduction zones, where an asperity on the subducting plate is tightly connected to the pore-collapse domain in the accretion wedge. In fact, Kumagai et al. (2012) showed that a strongly localized asperity, possibly a subducting seamount, may have been the origin of the mega-asperity of the 2011 Tohoku-Oki earthquake. Therefore, when a seamount on an oceanic plate encounters a rigid impermeable barrier layer in a continental plate, it might create the conditions for fault-valve behaviour to store deep Earth fluids during an interseismic period. This model might also be supported by recent physicochemical analyses of deep-sea waters performed after the 2011  $M_w$ 9 Tohoku-Oki earthquake, which showed that  $^{13}\text{C}$ -enriched methane and  $^3\text{He}$ -bearing fluids were released from deep sub-seafloor reservoirs after the mainshock passed through the plate interface in the subduction zone (Kawagucci et al. 2012; Sano et al. 2014).

When deep gases interact with the newly created crack surfaces generated in the fault valve, the unpaired electrons contained in the rock crystal defects are thermally stimulated (Fukuchi et al. 1986) and released into the open crack due to the rise in temperature ( $\geq 300\text{ }^\circ\text{C}$ ) at the crack tip via plastic work (Li et al. 1996). These electrons then become attached to the gas molecules, electrifying them to a negative state (Scudiero et al 1998; Enomoto 2012; Enomoto et al. 2017). We believe that this process is the elementary mechanism of the electromagnetic phenomena that accompanies an earthquake. Note that the geomagnetic variation caused by the 1965–1967 Matsushiro earthquake swarm could be explained quantitatively by this model (Enomoto et al. 2017).

The present report is an extension of previous laboratory experiments (Enomoto et al. 2017) performed to understand the electromagnetic phenomena underlying the quasi-static fracturing stage of the fault-valve zone. To this end, we conducted a wide range of experiments using various combinations of gas species and rock species, not only at the room temperature of  $25\text{ }^\circ\text{C}$  but also at an elevated temperature of  $160\text{ }^\circ\text{C}$ , a temperature comparable to that of the seismogenic zone (Sano et al. 2014). At this temperature, the rock still exhibits brittle properties (Kawamoto et al 1997), but unpaired electrons are stably trapped in the crystal lattice defects in the rock (Fukuchi et al. 1986).

## Methods

### Fracture tests

As illustrated in the schematic view of the experimental setup in Fig. 1a, a flat-ended V-shaped plate-type indenter made of hardened carbon steel was attached to a universal testing machine and pressed against a rock sample. The tested rocks were as-received quartz diorite (from Kanagawa/Tanzawa, Japan), gabbro (from Zimbabwe), basalt (from Hyogo, Japan), and fine-grained granite (from Fujian, China). The basic configuration of the equipment is the same as that previously reported (Enomoto et al. 2017), but

some improvements were made to conduct the experiment at elevated temperature ( $\approx 160$  °C) and under a variety of conditions.

A square rock sample was loosely clamped to prevent the edge of the rock from lifting during loading or jumping sideways upon rupture. Two sheets of polytetrafluoroethylene (PTFE) 0.4 mm thick were greased for lubrication and placed between the rock and the clamp stop surface to control the slippage during fracture so that the initial crack width at the time of fracture was about 1 mm (see Fig. 1b). At the same, a pressurized gas stored in a flow channel inside the indenter, which had an open slit 20 mm long by 1.8 mm wide, was sealed with a PTFE sheet 0.4 mm thick for experiments at room temperature of  $\approx 25$  °C (see Fig. 1b) and lead alloy sheet 0.4 mm thick for  $\approx 160$  °C (not shown). As shown on the right side of Fig. 1a, heated CO<sub>2</sub>, CH<sub>4</sub>, and N<sub>2</sub> gases at a pressure 0.4–0.5 MPa were supplied to the gas flow channel inside the indenter from the gas cylinders and passed through a temperature-controlled heat exchanger heated by hot water vapour supplied from a heated pressure vessel at the saturated vapour pressure. The indenter pressed the rock during loading at a crosshead speed of 0.5 mm/min, and immediately after the rock was subjected to a guillotine fracture at the critical fracture load, the gas flowed into the crack gap and interacted with the newly created fracture surface, resulting in electrification of gas molecules. Then, the gas current was measured by an electrode made of #20 copper mesh sputter-coated with platinum to prevent oxidation degradation (see Fig. 1c) and recorded by a datalogger with a sampling time of 10  $\mu$ s. The signal of the vibrometer attached to the indenter holder (see Fig. 1d) was used as a trigger to record the current and other signals to the datalogger.

In earlier experiments, it often happened that the fracture occurred irregularly outside the area directly below the gas outlet slit, and thus the current signal was also irregular. Therefore, a small flaw was introduced just under the slit with a diamond blade, and this produced the expected guillotine-type fracture with relatively good reproducibility. Its effectiveness was confirmed by finite element analysis of stress and strain under contact load, as described in the next section.

Several series of experiments were conducted to understand how the various factors affect the generation of electrified gas currents associated with rock fracture. These factors included gas species, rock species, rock/gas interaction area, and voltage bias on the electrode. The rock/gas interaction area  $S$  was defined as  $S = (\text{rock thickness } L_t) \times (\text{electrode width } L_w)$ .

In the first series of experiments to understand the characteristic feature of the signals from the acoustic emission (AE) sensor, the reference electrode and electrode for gas current were evaluated during the loading period up to the final fracture. Acoustic emissions were monitored at a rate of 500 counts/s and also the signal from the reference electrode, which was attached on the rock surface near the indenter, was measured to investigate the effect of space charge fluctuation during loading. The effect of bias voltages of 0 V, that is, an electrically floating state (no bias), and  $\pm 77$  V on the electrode was also evaluated.

In the second series, the effects of rock/gas interaction area  $S$  and various combinations of rock/gas species at gas temperatures of  $\pm 25$  °C and  $\pm 160$  °C on electric currents without the electrode bias were studied for quartz diorite, gabbro, and basalt.

In the third series, the electrical potential was measured using a contact-type ultra-high-impedance voltmeter attached to the electrically floating mesh electrode. The measuring range was  $\pm 0$ –2,000 V and the sampling time was 500  $\mu$ s. This experiment was performed with the combination of gabbro/N<sub>2</sub> at 160 °C. The electrostatic energy of the gas was then evaluated.

To investigate the electrostatic induction effect near the ground surface, away from the deep earthquake focal zone where coupled electrical interaction occurs, we conducted a fourth series of experiments with the setup shown in Fig. 1d and 1e. We filled an acrylic container with small granite grains and soil, and buried an electrode of stainless-steel rod 5 mm in diameter, with and without a non-conductive acrylic resin coating, at a depth 40 mm below the back surface of the fine-grained granite.

## Finite Element Analysis Of Elastic Deformation During Loading

Before adopting the flat-ended indenter described above, an R-tip indenter was used in preliminary experiments. However, the PTFE seat, which seals the pressurized gas, broke during loading due to high line contact stress, and the gas often leaked before the final fracture. Therefore, the flat-ended indenter was adopted to improve the sealing property.

However, there were often cases where the rock did not fracture directly under the gas slit of the indenter. Therefore, a flaw smaller than the slit width was introduced into the rock surface in the middle of the projection surface of the slit. We then conducted a finite element analysis to examine its effectiveness. To this end, we used SOLIDWORKS 2015® with the three-dimensional contact configuration shown in Fig. 1 f. The mesh size in the area where stress is concentrated, to a depth of 25 mm and with a width of 50 mm, was 0.3 mm, and the area outside the concentration had a mesh size of 4 mm (see Fig. 1g). The flaw size on the rock surface was 0.5 mm wide and 2 mm deep. The material parameters of the hardened carbon steel indenter and rock (granite) are noted in Fig. 1g.

Figure 1h is a colour chart showing the equivalent strain (ESTRN) level in Fig. 1i-1n, where Fig. 1i-1 k and 1 l-1n show the two-dimensional strain distribution along lateral line A-B (see Fig. 1f) at loads of 600, 800, and 1,200 kg without and with small flaws on the rock surface, respectively. The results show that when a flaw is introduced on the rock surface, the strain is well concentrated beneath the flaw at a load of 800 kg or more, which suggested that such flaws are likely to create a crack directly under the gas slit.

## Results And Discussion

# Characteristic feature of the signals during rock loading/fracture

In the first series of experiments using quartz diorite rock 20 mm thick with an attached AE sensor and an electrode biased at + 77 V with flowing CO<sub>2</sub> gas (hereafter we simply note this as “combination of quartz diorite/CO<sub>2</sub>”), the typical results (Fig. 2a) showed that the AE signal began to appear from the start of loading, gradually decreased as the load increased, and completely disappeared before the final rupture of the rock. The average fracture load of five tests was 925 kg, while the maximum load, where the AE signals disappeared, was 0.58 of the fracture load on average. This is likely because inelastic deformation due to void collapse and/or grain boundary slip, which caused the AE, were completed when the load reached about 0.6 times the fracture load. Then, elastic deformation proceeded until the final fracture. The inelastic processes were related to AE generation that were less affected the gas current signal.

As shown in Fig. 2b, the electrified gas current was successfully measured for approximately 100 μs after the full development of the crack when a big vibration occurred (see the grey signal in Fig. 2b). Note that the pico-ammeter displays the negatively charged current signal on the upper side on the datalogger. To determine how the fluctuation of the space charge noise during loading affects the current signal, the signal of the electrode placed near the indenter, as shown in the inset of Fig. 2b, was monitored. The result indicated that the space charge effect was much less, as shown by the orange signal in Fig. 2b. Note that laboratory experiments of the electric currents due to stress-activated effects (Hadjicontis and Mavromatou 1996; Freund 2002; Dahlgren et al. 2014) or due to water-induced electrokinetic effects (Wang et al. 2015) in rocks have been reported. The current levels were on the order of several to several tens of nanoamperes. In comparison to these reported results, the present gas currents were an order of magnitude more.

Figure 2c and 2d show typical electric current signals measured at an electrode bias of ± 77 V for the combination of quartz diorite/CO<sub>2</sub> at 25 °C, and ± 77 V and no bias for the combination of gabbro/CO<sub>2</sub> at 160 °C, respectively. These results show that the current was less related to the polarity of the electrode bias voltage under the present conditions. Because all signals were recorded on the positive side even without bias, the current should be negatively charged. Thus, the results suggest that the charged gas current has negative potential higher than - 77 V, which was confirmed by the experiments described in the next section.

## Effect of rock/gas interaction area, rock and gas species, and gas temperature

In the next series of experiments, a bias-free electrode was used to investigate the effect of rock/gas interaction area  $S$  and the gas species at 25 °C and 160 °C for gabbro and basalt. Figure 3a shows the current signals of  $S = 1.2 \times 10^{-4} \text{ m}^2$  (i.e.,  $L_t = 15 \text{ mm}$  and  $L_w = 8 \text{ mm}$ ) and  $2.4 \times 10^{-4} \text{ m}^2$  (i.e.,  $L_t = 20 \text{ mm}$  and

$L_w=12$  mm) for the combination of gabbro/ $\text{CH}_4$  at  $\approx 160$  °C, and it can be seen that the peak current increased as the interaction area  $S$  increased.

Figure 3b shows the current measurements conducted twice each for the combination of gabbro/ $\text{CO}_2$  at  $\approx 25$  °C and  $\approx 160$  °C. The peak currents were all in the range 0.08–0.15  $\mu\text{A}$  and independent of the temperature. The reproducibility of the signals is also considered to be reasonable.

Figure 3c shows a comparison of the currents for gabbro combined with various gas species – water vapour,  $\text{CO}_2$ ,  $\text{N}_2$ , and  $\text{CH}_4$  at  $\approx 160$  °C – and also the current for basalt combined with  $\text{N}_2$  at  $\approx 160$  °C. The interaction area  $S$  was  $1.2 \times 10^{-4}$   $\text{m}^2$  in these experiments. The results show that the gas current characteristics did not change regardless of the rock and gas species combination.

Figure 3 summarizes the relationship between the peak current  $I_p$  of various gases at  $\approx 25$  °C and  $\approx 160$  °C for quartz diorite and gabbro in the present experiments, as well as the peak current  $I_p$  of quartz diorite/ $\text{CO}_2$  at  $\approx 25$  °C reported elsewhere (Enomoto et al. 2017) and the interaction area  $S$ . As  $S$  increased, the scatter in the peak current  $I_p$  became notable because the increasing thickness of the rock  $L_t$  or width of the electrodes  $L_w$  often causes unstable or irregular rock fractures. Nevertheless, the relationship of  $I_p$  versus  $S$  could be expressed by a linear approximation:  $I_p$  (in microamperes) =  $1,069 \times S$  (in square meters) with the decision coefficient  $R^2 = 0.83$ , which indicated the maximum current density per 1  $\text{m}^2$  of fracture area is 1.1  $\text{mA}/\text{m}^2$ , regardless of the rock or gas species, gas temperature and pressure, or bias of the electrode in the range tested in the second series of experiments.

## Electrostatic Energy

To estimate the electrostatic energy of the electrified gas flow in the present fracture experiments, we independently measured the current flowing through the electrode and the potential generated on the electrically floating electrode for the combinations of gabbro/ $\text{N}_2$  and gabbro/ $\text{CH}_4$ . Figure 4a and 4b show the typical current results for the combinations of gabbro/ $\text{N}_2$  and  $\text{CH}_4$  at  $\approx 160$  °C and electric potential for the combination of gabbro/ $\text{N}_2$  at  $\approx 160$  °C, respectively. From Fig. 4a, the total negative charge  $Q$  generated during the total time from the first increase of the current signal to its peak at 4,570  $\mu\text{s}$  is estimated as  $-5.3 \times 10^{-12}$  C, and from Fig. 4b, the maximum potential  $V$  is -230 V. The electrostatic energy  $E$  is thus estimated as

$$E = \frac{1}{2}QV = \frac{1}{2} \times (-5.3 \times 10^{-12} \text{ C}) \times (-230 \text{ V}) = 1.3 \times 10^{-9} \text{ J}.$$

In some of the gabbro fracturing experiments using  $\text{CH}_4$ , the rock fracturing test section was shielded from external light with a blackout curtain, and a high-sensitivity camera with ISO 12,400 was used to take a photograph and determine whether the electrostatic ignition of flammable  $\text{CH}_4$  occurred during the final rock fracture, but ignition could not be confirmed. Because the minimum energy for electrostatic ignition of  $\text{CH}_4$  is at least  $0.3 \times 10^{-3}$  J (Pratt 2000), an experiment as large as  $0.3 \times 10^{-3} / 1.3 \times 10^{-9} = 2.3 \times 10^5$

times the present scale might be required for electrostatic ignition of CH<sub>4</sub>. Because the fracture area interacting with CH<sub>4</sub> in the present experiment was  $1.2 \times 10^{-4} \text{ m}^2$ , there is a high probability that CH<sub>4</sub> would be electrostatically ignited by the fracture of  $(1.2 \times 10^{-4} \text{ m}^2) \times (2.3 \times 10^5) = 27.6 \text{ m}^2$  or more, which corresponds to a fracture size of about  $5.3 \text{ m}^2$ . This suggests that, because fractures of this scale can easily occur at the fault zone due to tectonic stress during an earthquake, deep Earth CH<sub>4</sub> gas is likely to ignite electrostatically.

## Electrostatic Induction

From the fourth series of experiments, Fig. 4c shows typical gas currents at a temperature of  $\approx 25 \text{ }^\circ\text{C}$  with  $S = 1.2 \times 10^{-4} \text{ m}^2$  for the combination of granite/CO<sub>2</sub> as well as that of gabbro and quartz diorite/CO<sub>2</sub> for comparison. Figure 4d shows the induced current collected by the rod electrodes with and without resin coating buried in the container (see Fig. 1e). First, we discuss the results in Fig. 4c, where it is noted that the peak current  $I_p$  of the granite is about 10 times larger than those of quartz diorite and gabbro. The average peak current of four tests for granite was  $1.76 \pm 0.36 \text{ mA}$ . One possible reason for this difference is that granite contains more exoelectron emission sources, that is, unpaired electron sites at lattice defects, than the other rocks. To confirm this, we performed electron spin resonance (ESR) analyses to detect trapped electrons at the lattice defects, such as the E' centre in granite and quartz diorite. However, a normal ESR spectrum could not be obtained, possibly because iron ions or some other metal ions in the rocks interfered with normal ESR acquisition. As the exoelectrons captured at the lattice defects are caused by radioactive elements within the rock, we measured the  $\gamma$ -ray equivalent dose rate from the present rock samples using an environmental radiation monitoring device (measuring range of 150–1,250 KeV and 0.001–9.999 mSv/h, sampling period of 1.6 min). Figure 4e shows the typical dose equivalent rate of quartz diorite, gabbro, and granite for the measurement period of 30 min in open air. The number of events, defined as the peak dose equivalent rate  $N_{Y>0.04}$  exceeding  $0.04 \text{ } \mu\text{Sv/h}$  for 30 min, were counted. The results of  $[N_{Y>0.04}(\text{rock})] - [N_{Y>0.04}(\text{background}) = 1]$  were 4 for quartz diorite, 3 for gabbro, 7 for basalt, and 46 for fine-grained granite, where  $N_{Y>0.04}$  for granite is the highest among the rock samples. The peak currents and the  $N_{Y>0.04}$  number for the rocks are compared in Fig. 4 f. The fact that the correlation between the  $I_p$  and  $N_{Y>0.04}$  of each rock is high suggests the validity of the present working hypotheses: the origin of the gas current after coupled interaction of fracturing rock can be attributed to the mechanism of exoelectron release from the newly created cracked surface plus the electrification of gas molecules due to electron attachment reactions.

Next, we discuss the results of Fig. 4d, where electrostatic induction signals were successfully detected by an electrode made of stainless-steel rod buried in a container filled with rock grains/soil. Note that the signal of Fig. 4c is a negatively charged gas current, while that of Fig. 4d is the opposite, which means that a positive charge is electrostatically induced on these electrodes, even with an insulation coating. The present experiment does not necessarily simulate the geometrical scale between the focal zone of an earthquake and the ground surface, but it does suggest that the negative charges generated during the

quasi-static fracture process of the focal zone can induce positive charges in an electrode buried near the ground surface. These results thus provide an explanation for previous observations of anomalous changes in telluric current in the precursor stage of earthquakes (e.g., Varotsos and Lazaridou 1991; Varotsos et al. 1993; Nagao et al. 1996; Enomoto et al. 2006).

## **Conclusion**

The present experiments demonstrated that deep gases, which invade cracks extending through the fault-valve zone and flow upward, interact with quasi-static fractures in the earthquake focal zone to form a negatively charged current after electrical interaction with the newly created cracked surfaces. The current magnitude is larger for rocks that contain lattice defects that capture unpaired electrons produced through geological time by natural radiation arising from the decay of radioactive elements (e.g., granite). The fracture-induced gas current was much higher than the stress-induced current and the electrokinetic streaming current previously reported. It was also experimentally confirmed that the flow of negatively charged gas generated at the focal zone deep underground can induce positive charges at the ground level. The present results thus suggest a mechanism for the previously reported anomalous signals in telluric current that are often observed at the ground level in association with earthquakes.

## **Declarations**

### **Acknowledgements**

We thank Genesis Research Institute, Inc., for the collaborative support on the present work.

### **Author's contribution**

YE planned the research and prepared the manuscript. TY and YE performed fracture experiments. SS and HK contributed to project administration. All authors read and approved the final manuscript.

### **Funding**

This project was supported by Genesis Research Institute Inc.

### **Availability of data and materials**

The datasets used and/or analysed during the current study are available from the corresponding author on reasonable request.

### **Competing interests**

The authors declare no competing interests.

### **Author details**

<sup>1</sup> Fii, Ueda Campus, Shinshu University, 3-15-1 Tokida, Ueda, Nagano 386-8567,

Japan.

<sup>2</sup> Genesis Research Institute, Inc, 4-1-35 Noritake-Shinmachi, Nishi-ku, Nagoya, Aichi 451-8567, Japan.

Received:

Accepted:

## References

Dahlgren RP, Johnston MJS, Vanderbilt VC, Nakaba RN (2014) Comparison of the stress simulated current of dry and fluid-saturated gabbro samples. *Bull Seismo Soci Ameri* 104:2662-2672.

doi:10.1785/0120140144

Enomoto Y, Hashimoto H, Shirai N, Murakami Y, Mogi T, Takada M, Kasahara M (2006) Anomalous geoelectric signals possibly related to the 2000 Mt. Usu eruption and 2003 Tohoku-Oki earthquakes. *Phys Chemi Earth* 31:319-324. doi:10.1016/j.pce.2006.02.013

Enomoto Y (2012) Coupled interaction of earthquake nucleation with deep Earth gases: a possible mechanism for seismo-electromagnetic phenomena. *Geophys J Iner* 191:1210-1214.

doi:10.1111/j.1365-246X.2012.05702.x

Enomoto Y, Yamabe T, Okumura N (2017) Causal mechanisms of seismo-EM phenomena during the 1965-1967 Matsushiro earthquake swarm. *Sci Rep* 7:44774. doi.org/10.1038/srep44774

Freund FT (2002) Charge generation and propagation in igneous rocks. *J Geodyn* 33:543-570.

doi:10.1016/S0264-3707(02)00015-7

Fukuchi T, Imai N, Shimokawa K (1986) ESR dating of fault movement using various defect centers in quartz; the case in the western South Fossa Magna, Japan. *Earth Planet Sci Lett* 78:121-128.

doi.org/10.1016/0012-821X(86)90178-0

Gold T (1987) Outgassing in solid rock, in *Power from the Earth*. JM Dent & Sons Ltd. London, 78-91.

Hadjicontis V, Mavromatou C (1996) Laboratory investigation of the electric signals preceding earthquakes. *A Critical Review of VAN*, J Lighthill ed, World Sci 105-117.

doi.org/10.1142/9789812815491\_0006

Kawagucci S, Yoshida YT, Noguchi T, Honda, MC, Uchida H, Ishibashi H, Nakagawa F, Tsunogai U, Okamura K, Takaki Y, Nunoura T, Miyazaki J, Hirai M, Lin W, Takai K (2012) Disturbance of deep-sea environments induced by the M9.0 Tohoku earthquake, *Sci Rep* 2:270. doi:10.1038/srep00270

- Kawamoto E, Shimamoto T (1997) Mechanical behavior of halite and calcite shear zones from brittle to fully-plastic deformation and a revised fault model. *Structural Geology and Geomechanics Proc. 30<sup>th</sup> Int'l Geol. Congr. Vol 14:89-105.* doi.org/10.1201/9780203738061
- Kumagai H, Pulido N, Furuyama E, Aoi S (2012) Strong localized asperity of the 2011 Tohoku-Oki earthquake, Japan. *Earth Planets Space 64:649-654.* doi:10.5047/eps.2012.01.004
- Li W, Deng X, Rosakis A (1996) Determination of temperature field around a rapidly moving crack-tip in an elastic-plastic solid, *Inter J Heat Mass Transfer 39:677-690.* doi.org/10.1016/0017-9310(95)00175-1
- Nagao T, Uyeda S, Asai Y, Kono Y (1996) Anomalous changes in geoelectric potential preceding four earthquakes in Japan. A critical review of VAN. J Lighthill ed, *World Sci 292-300.* doi.org/10.1142/9789812815491\_0006
- Sano Y, Hara T, Takahata N, Kawaguchi S, Honda MC, Nishino Y, Tanikawa W, Hasegawa A, Hattori K (2014) Helium anomalies suggest a fluid pathway from mantle to trench during the 2011 Tohoku-Oki earthquake. *Nat Commun 5:3084.*doi:10:1038/ncomms4084
- Sano Y, Takahata N, Kagoshima T, Shibata T, Onoue T, Zhao D (2016) Groundwater helium anomaly reflects strain change during the 2016 Kumamoto earthquake in Southwest Japan. *Sci Rep 6:37939.* doi:10.1038/srep37939
- Sibson R (1990) Conditions for fault-valve behaviour. *Geol Soc London Spec Pub 54:15-28.* doi:10.1144/GSL.SP.1990.054.01.02
- Smithson SB, Wenzel F, Granchin YV, Morozon IB (2000) Seismic results at Kola and KYB deep scientific boreholes: velocities, reflections, fluids, and crustal composition. *Tectonophy 329:301-317.* doi:10.1016/S0040-1951(00)00200-6
- Scudiero L, Dickinson T, Enomoto Y (1998) The electrification of flowing gases by mechanical abrasion. *Phys Chem Minerals 25:566-573.* doi:10.1007/s002690050149
- Pratt TH (2000) Electrostatic ignitions of fires and explosions. *CCPS of the Ameri. Inst. Chem.Eng. New York Chap 4, 182.*
- Varotsos P, Lazaridou M (1991) Latest aspects of earthquake prediction in Greece based on seismic electric signals. *Tectonophys 188:321-347.* doi.org/10.1016/0040-1951(91)90462-2
- Varotsos P, Alesopoulos K, Lazaridou M (1993) Latest aspects of earthquake prediction in Greece based on seismic electric signals II. *Tectonophys 224:1-37.* doi.org/10.1016/0040-1951(91)90462-2
- Wang J, Hu H, Guan W, Li H (2015) Electrokinetic experimental study on saturated rock samples: Zeta potential and surface conductance. *Geophys J Inter 201:869-877.* doi:10.1093/gji/ggv013

# Figures

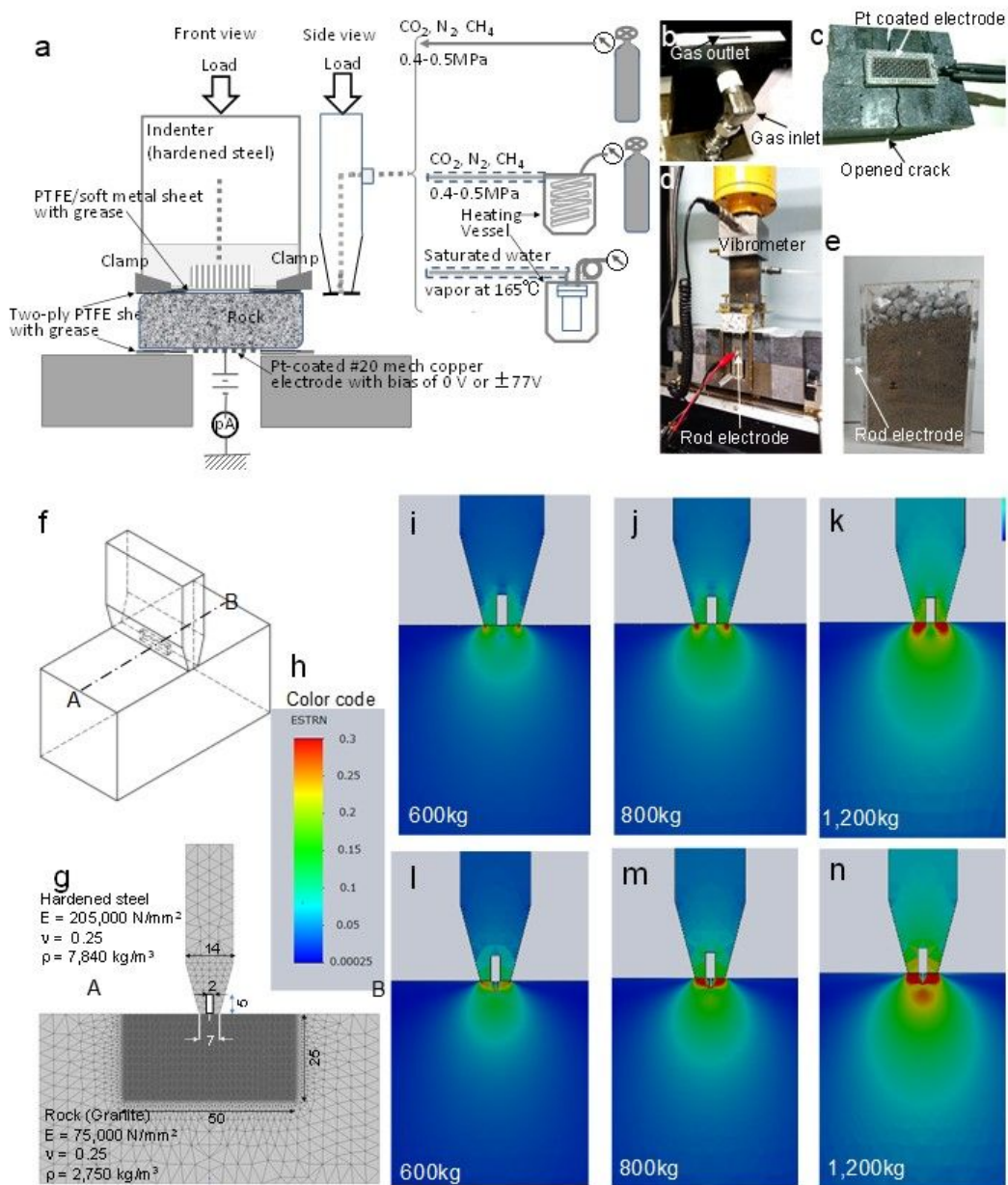


**Figure 1**

a) Schematic view of the experimental setup: universal tester for the measurement of electrified gas current interacting with fractured rock at temperatures of  $\approx 25^\circ\text{C}$  and  $\approx 160^\circ\text{C}$ , with the three methods of gas supply shown on the right side; b) flat-ended indenter gas outlet (slit) covered with PTFE seal, as seen

from below; c) bottom view of Pt-coated mesh electrode attached to the underside of the rock; d) setup in fourth series of experiments with an electrode (stainless steel rod with or without resin coating) buried in acrylic container filled with granite grains and soil; e) close-up of container in d); f) three-dimensional model of flat-ended indenter on a rock; g) meshing for model shown in f), with contact configuration, mesh refinement near stress concentration, line A-B, and parameters; h) colour coding of equivalent strain; and i-k) and l-n) two-dimensional strain distribution along a line A-B at loads of 600, 800, and 1,200 kg without and with a small flaw on the rock surface, respectively.

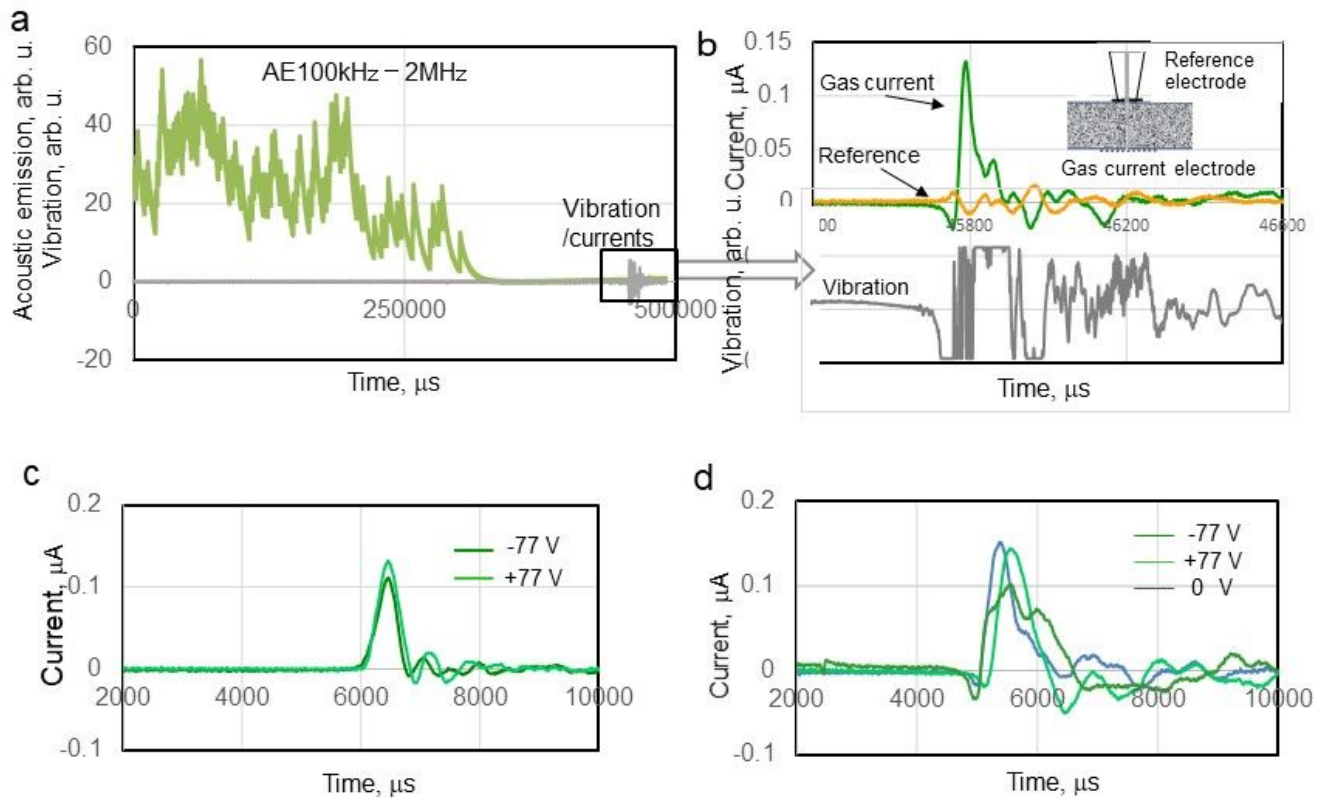


**Figure 2**

a) AE, vibration, and current signals for combination of quartz diorite/CO<sub>2</sub> at 25 °C with electrode bias of +77 V and  $S=1.6 \times 10^{-4}$  m<sup>2</sup>; b) enlargement of area surrounded by the square in a), where green curve is the signal at the gas current electrodes, orange curve is the signal at the reference electrode, and grey curve is the vibration signal; c) current for quartz diorite/CO<sub>2</sub> at 25 °C with electrode bias of  $\pm 77$  V; and d) current for gabbro/CO<sub>2</sub> at 160 °C with electrode bias of  $\pm 77$  V and without bias (0 V). In all tests,  $S=1.2 \times 10^{-4}$  m<sup>2</sup>.

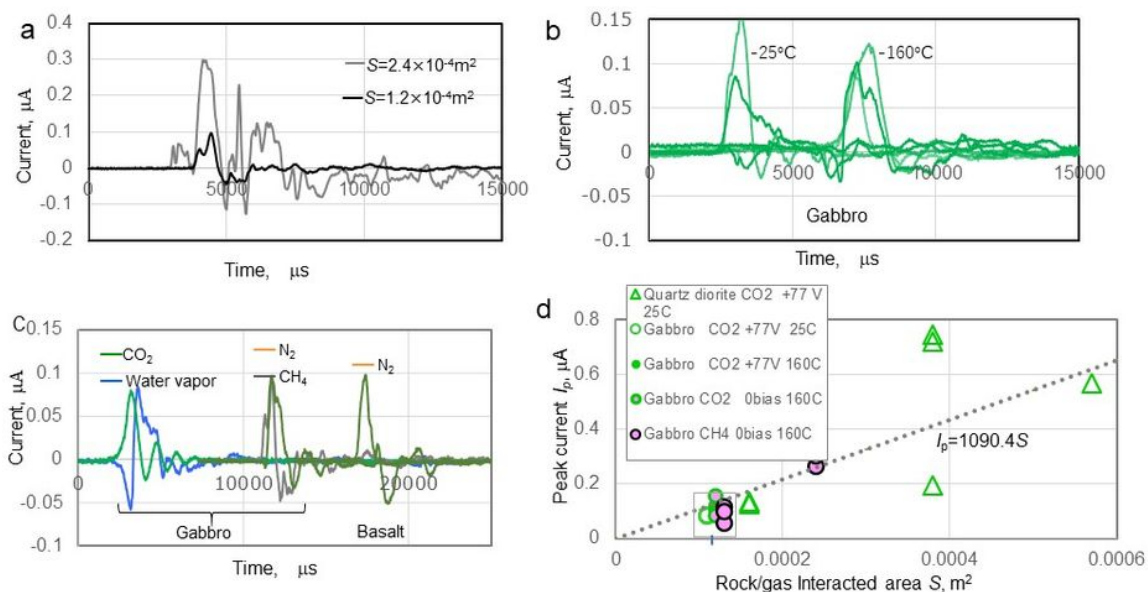


**Figure 3**

a) Electric currents for combination of gabbro/CH<sub>4</sub> at 160 °C without electrode bias at  $S=1.2 \times 10^{-4} \text{ m}^2$  and  $S=2.4 \times 10^{-4} \text{ m}^2$ ; b) electric currents for combination of gabbro/CO<sub>2</sub> at 25 °C and 160 °C (two signals for each temperature overlap because two tests were performed at each temperature to check the reproducibility); c) electric signals for combination of gabbro and CO<sub>2</sub>, water vapour, N<sub>2</sub>, and CH<sub>4</sub> at 160 °C and combination of basalt and N<sub>2</sub> at 160 °C; and d) relationship between the peak current  $I_p$  and rock/gas interaction area  $S$  for the various test conditions listed in the plot legend. The dotted line in d) is an approximated relation:  $I_p (\mu\text{A})=1,069 \times S (\text{m}^2)$ , where the decision coefficient  $R^2=0.83$ .

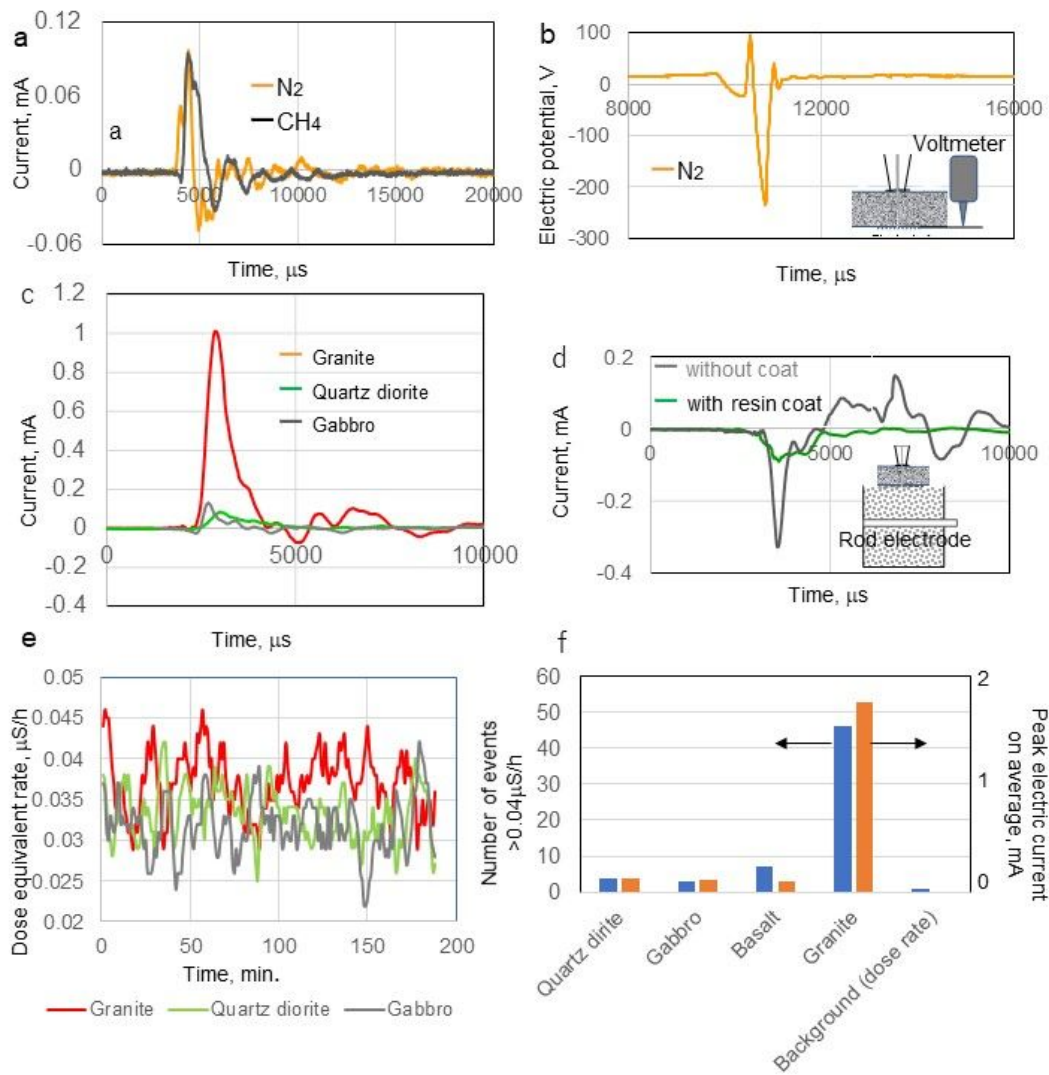


**Figure 4**

a) and b) Typical results for third series of experiments: a) currents for combination of gabbro/CH<sub>4</sub> or N<sub>2</sub> at 160 °C and b) electric potential for gabbro/N<sub>2</sub> at 160 °C. c) and d) Typical results for fourth series of experiments: c) current and vibration for combination of granite/CO<sub>2</sub> at 25 °C and d) induced current signals at the pipe electrode with and without non-conductive resin coating buried in a container filled with granite grains and soil. e)  $\gamma$ -Ray equivalent dose rate for granite, gabbro, and quartz diorite in 30-min

measurements. f) Comparison number  $N_{\gamma > 0.04}$  of events for the  $\gamma$ -ray equivalent dose rate greater than  $0.04 \mu\text{Sv/h}$  and average peak currents for several test runs of quartz diorite, gabbro, basalt, and granite with  $\text{CO}_2$  at  $S=1.2 \times 10^{-4} \text{ m}^2$  and temperature of  $\pm 25 \text{ }^\circ\text{C}$ ;  $N_{\gamma > 0.04}$  for the background in open air is also included.

## Supplementary Files

This is a list of supplementary files associated with this preprint. Click to download.

- [Abstractimage.jpg](#)